Oscillating grid Turbulence: The influence of Reynolds number and forcing

Oscillating grid Turbulence: the influence of Reynolds number and forcing

Journal of Physics: Conference Series **3173** (2026) 012043 doi:10.1088/1742-6596/3173/1/012043

Oscillating grid Turbulence: the influence of Reynolds number and forcing

Michele Iovieno[1], Holger Foysi[2] and George Khujadze[2]

[1]Politecnico di Torino, Dipartimento di Ingegneria Meccanica e Aerospaziale, Torino, Italy
[2]University of Siegen, Chair of Fluid Dynamics, Siegen, Germany

E-mail: michele.iovieno@polito.it

Abstract. Direct numerical simulations are performed to study turbulence generated by oscillating grids, modeled by a localized body forcing. The flow exhibits three distinct regions: (i) a homogeneous turbulent core, (ii) a transport-dominated zone with algebraic decay, and (iii) an interfacial layer where the turbulent kinetic energy decreases exponentially. Velocity spectra in the core region develop a Kolmogorov-like inertial subrange, confirming the establishment of fully developed turbulence. The results show persistent anisotropy, with grid-normal velocity fluctuations exceeding parallel components across all Reynolds numbers, in contrast to classical freely decaying turbulence. The energy decay exponents depend on the geometry and forcing of the grid and agree with the broad scatter reported in experimental studies. These findings indicate that oscillating-grid turbulence is reproducible but non-universal, providing a controlled configuration for the study of entrainment, mixing, and scalar transport.

1 Introduction

In this work, we investigate the propagation of turbulence generated by an oscillating grid in an otherwise quiescent fluid, by means of direct numerical simulations (DNS). Oscillating grids have long been used in laboratory experiments as a controlled method to produce statistically steady turbulence. This flow configuration is distinctive in that turbulent diffusion can be studied in relative isolation from turbulent production. It also represents one of the simplest examples of a statistically steady yet inhomogeneous turbulent flow, whose properties depend primarily on the distance from the grid. Despite this apparent simplicity, the flow exhibits a complex structure: a production region close to the grid, where energy is injected by its motion; an intermediate region in which turbulence propagates; and an interface region that advances into the surrounding still fluid through entrainment.

Experimentally, oscillating–grid turbulence (OGT) is generated by a planar grid driven sinusoidally or almost sinusoidally within a sufficiently large tank, typically at small amplitude and high frequency. Under these conditions, the balance between turbulent diffusion and viscous dissipation sustains a statistically stationary turbulent field. This configuration has been extensively used as a model flow to study mixing in stably stratified fluids, interfacial gas transfer at the air–water surface [1], and turbulence modulation by suspended particles [2]. However, compared to canonical shear flows, oscillating–grid turbulence has received comparatively little attention. Pioneering experimental studies include those of Hopfinger and co-workers [3, 4] and De Silva [5], who documented the principal features of OGT. In such flows, turbulence originates from the interaction of the jets and wakes shed by the oscillating grid bars. Ideally, no significant mean flow is present, and turbulence may be considered approximately homogeneous in

planes parallel to the grid. As shown in the cited literature above, the turbulent region is separated from the surrounding irrotational fluid by a sharp turbulent/non-turbulent interface (TNTI).

The distinctive properties of OGT have also motivated numerical investigations. Yang et al. [6] employed a pseudo-spectral code with periodic boundary conditions in the horizontal directions, introducing a localized forcing designed to mimic the action of the oscillating grid. However, their simulations were hindered by a coarse vertical resolution that limited the accuracy of the results. Godeferd et al. [7] performed DNS using a similar approach but implemented a more physically realistic forcing, localized in a plane, which allowed them to reproduce the effect of grid parameters such as mesh size, amplitude, and oscillation frequency. Their work reached grid Reynolds numbers, based on stroke length and frequency of grid oscillations, of about 1,100 in the non rotating case and, even if resolution was too coarse to capture all scales of the flow, demonstrated that the specific form of the forcing plays a crucial role in determining the ensuing turbulence.

A number of scaling laws have been proposed to describe the turbulence in the intermediate region of OGT. However, the dependence of these scaling behaviors on the grid Reynolds number and on the precise form of the forcing remains insufficiently clarified, yet. The objective of the present study is to address this problem. Using DNS, we investigate how the statistically steady, asymptotic state of oscillating–grid turbulence depends on the grid Reynolds number and on the formulation of the forcing. We explore a wide range of Reynolds numbers and distinct forcing strategies, with the aim of disentangling their respective influence on turbulence generation, propagation, and scaling.

2 Physical model and numerical method

2.1 Governing equations

We consider a Cartesian reference frame with the x_3 axis normal to the grid plane, and the origin at the grid mean position, so that the plane $x_3 = 0$ corresponds to the grid location. The grid has a periodicity (mesh size) M in both x_1 and x_2 directions, and oscillates normally in its plane with stroke length S and angular frequency n. An illustration of the flow configuration and computational domain is presented in plot (a) in Figure 1.

The flow is governed by the incompressible Navier–Stokes equations. Using M as the characteristic length, $1/n$ as the time scale, and $\rho_0 M^2 n^2$ as the pressure variation scale, one can define the dimensionless time, position, velocity, and pressure as

$$t^* = nt, \qquad \boldsymbol{x}^* = x/M, \qquad \boldsymbol{u}^* = \boldsymbol{u}/(Mn), \qquad p^* = (p - p_0)/(\rho_0 M^2 n^2),$$

respectively, where p_0 is the pressure of the undisturbed ambient. The equations can consequently be written in dimensionless form as

$$\begin{aligned} \nabla_* \cdot \boldsymbol{u}^* &= 0, \\ \frac{\mathrm{D}\boldsymbol{u}^*}{\mathrm{D}t^*} &= -\nabla_* p^* + \frac{1}{\mathrm{Re}_M} \nabla_*^2 \boldsymbol{u}^* + \boldsymbol{f}^*(t^*, \boldsymbol{x}^*), \end{aligned}$$

where $\mathrm{Re}_M = M^2 n/\nu$ is the grid Reynolds number, and $\boldsymbol{f}^*$ is the forcing term.

2.2 Forcing formulation

The forcing mimics the momentum input from the oscillating grid. It is localized around $x_3 = 0$ and defined as

$$f_i^*(t^*, \boldsymbol{x}^*) = \frac{S^*}{2} \left[G(x_1^*, x_2^*)\, \delta_{i3} + \frac{\beta_i}{4} \right] g(x_3^*)\, \mathrm{e}^{it^*}, \tag{1}$$

where $S^* = S/M$ is the dimensionless stroke length. The function $G(x_1^*, x_2^*)$, which is double periodic with unit period in both variables, prescribes the horizontal distribution of forcing, acting only in the x_3 direction, while the random coefficients $\beta_i \in [-1, 1]$ introduce small perturbations following the approach of Godeferd et al. [7]. Vertical localization is achieved by a Gaussian function $g(x_3^*)$ centered on $x_3 = 0$. Two forms of G are considered:

$$\begin{aligned} G_1(x_1^*, x_2^*) &= 1 - \cos^2(\pi x_1^*)\, \cos^2(\pi x_2^*)\,, \\ G_2(x_1^*, x_2^*) &= \left|\cos(\pi x_1^*)\, \cos(\pi x_2^*)\right|\,. \end{aligned}$$

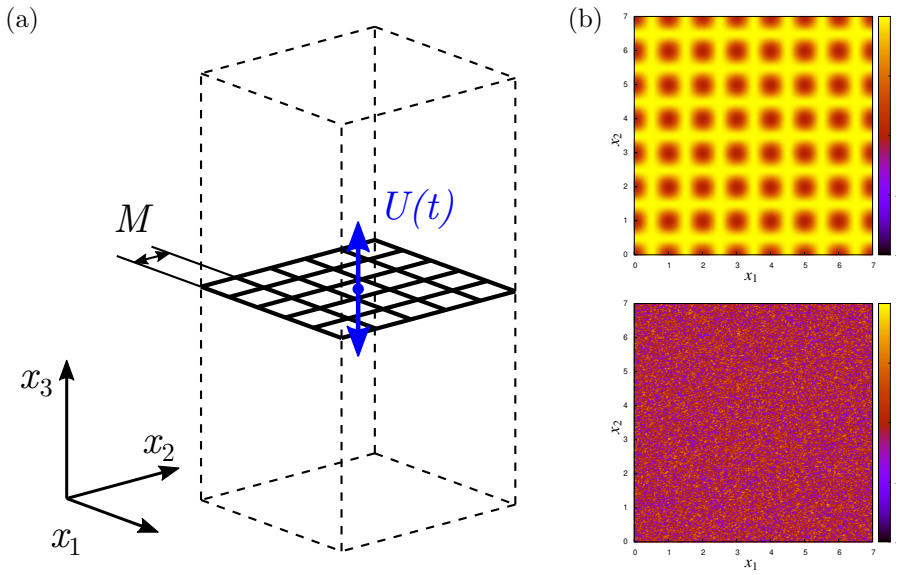

Figure 1: (a) Illustration of the flow configuration and computational domain. (b) Example of forcing component f_3 in the grid normal direction: on top the amplitude of the deterministic part of the forcing $G_1(x_1, x_2)$, below a realization of the random part.

For any chosen grid function G, the problem is thus characterised by two non-dimensional parameters: the grid Reynolds number Re_M, and the stroke-to-mesh ratio S^*. The latter determines the energy injection rate, proportional to $\langle f_i^* u_i^* \rangle$. In this work, we fix $S^* = 1$ and vary Re_M.

A scheme of the flow configuration is presented in Figure 1(a), together with an example of the forcing component f_3 in the normal direction of the grid in plots (b) in Figure 1. The amplitudes of the deterministic and random parts are shown in the top and bottom plots, respectively.

2.3 Numerical method

The governing equations are solved by direct numerical simulation using a Fourier–Galerkin spectral method, with periodic boundary conditions in all three directions. This choice ensures spectral accuracy in space and simplifies the solution of the pressure Poisson equation, which is carried out exactly in Fourier space. Nonlinear terms are evaluated in physical space with the pseudo-spectral method, and dealiasing is enforced by the standard 2/3 rule. Time integration is performed with a fourth-order explicit Runge–Kutta scheme for the non-linear terms. The present solver is derived from the Fourier–Galerkin spectral code of Iovieno, Cavazzoni and Tordella [8], modernized with a modular structure. The main algorithmic difference is the use of a standard four-step fourth-order Runge–Kutta scheme for time advancement (with projection onto a solenoidal field at each sub-step) instead of the original low-storage Runge–Kutta method. Since the timestep restriction is set by advective stability at the Reynolds numbers of interest, this fully explicit integration is adequate.

The computational domain has dimensions $L_1 \times L_2 \times L_3$, with $L_1 = L_2$ large enough to contain several grid meshes in the x_1 and x_2 directions, and L_3 chosen sufficiently large so that turbulence generated in the forcing plane remains well separated from its periodic image. The fictitious grid is placed in the center of the domain in the x_3 direction. All simulations have been performed with $L_1^* = L_2^* = 7$ and $L_3^* = 21$. Resolutions of $256 \times 256 \times 1536$ and $384 \times 384 \times 2304$ collocation points are used, enough to satisfy, a posteriori, the condition $k_{\max}\eta > 1.5$, where η is the Kolmogorov length scale, to ensure that all dynamically relevant scales are resolved. Simulations are initialized from rest and processed through the initial transient until the flow reaches a statistically stationary state. Statistics are then accumulated over several hundred oscillation periods, with averages performed in both time and in planes parallel to the grid.

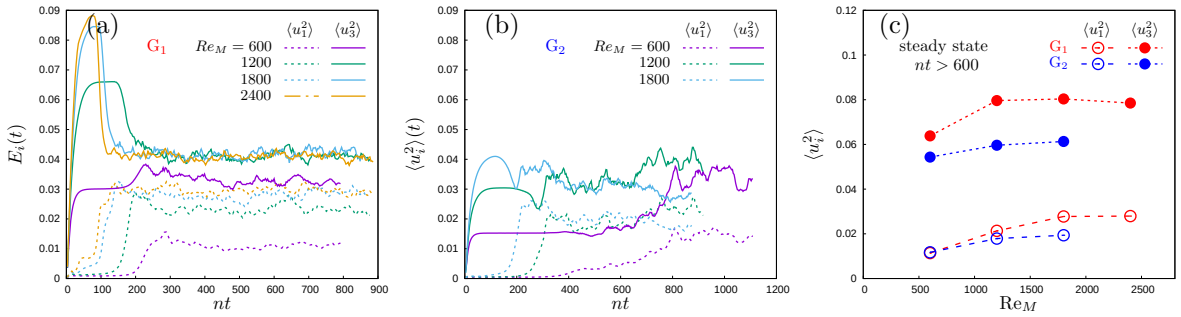

Figure 2: Time evolution of the integrated velocity moments E_1 and E_3 for grids (a) G_1 and (b) G_2, and (c) their ratio E_3/E_1. The transient adjustment is longer for grid G_1, while grid G_2 reaches its asymptotic state more rapidly. In all cases the turbulence remains anisotropic, with persistent excess energy along the grid-normal direction.

3 Results

First, the global energetics of the flow through integrated velocity moments are examined, which allows the assessment of the approach to reach a statistically stationary state and investigates the persistence of anisotropy. Second, an analysis of the spatial distribution of the turbulent kinetic energy is performed as a function of the distance from the grid, highlighting the emergence of distinct regions of turbulence decay. Third, the spectral properties of the velocity field are studied, with a focus on the existence and extent of the inertial-range scaling. Finally, a wavelet decomposition of the vorticity field is used to separate coherent and incoherent contributions, thus revealing the imprint of the forcing on the far-field flow.

3.1 Global evolution and anisotropy

Figure 2 depicts the time evolution of the integrated second-order velocity moments,

$$E_i(t) = \int_0^\infty \langle u_i^2 \rangle(t, x_3)\, \mathrm{d}x_3, \tag{2}$$

which quantify the kinetic energy contained in each velocity component. Following an initial transient phase characterised by strong oscillations, the moments gradually stabilise and approach an asymptotic plateau. This behavior indicates that the flow reaches a quasi-steady turbulent regime after the initial adjustment to grid forcing. The transient is markedly longer for grid G_1, whose higher blockage ratio produces stronger oscillatory motions, compared with grid G_2.

The ratio of the normal to the parallel components (Fig. 2c) reveals that the turbulence remains anisotropic, with the grid-normal energy consistently larger than the parallel components. This anisotropy does not vanish with time but instead reaches a statistically stationary value, confirming that oscillating grids sustain quasi-isotropic fluctuations only in an approximate sense, with a persistent energetic preference along the forcing direction.

3.2 Spatial distribution of kinetic energy

The spatial distribution of second-order moments is shown in Figure 3, plotted for different non-dimensional times nt. A distinct three-zone structure emerges. (i) A central homogeneous core close to the grid exhibits nearly uniform turbulent kinetic energy, signifying vigorous mixing and isotropic-like turbulence. (ii) A convective transport region follows, where the turbulent kinetic energy decreases with distance from the grid following a power-law dependence. Here, turbulent fluctuations are progressively diluted into the surrounding quiescent fluid. (iii) Finally, an interfacial region is observed at large distances, where the moments decay exponentially. This thin layer reflects a balance dominated by viscous diffusion and engulfment processes, in the absence of local production.

The extent of each region depends on the forcing parameters. At lower Reynolds numbers (Re_M=600) the extent of the convective tranport region for Grid G_1 strongly depends on the non-dimensional time. Initially, a quick extension is observed leading to a short saturation until $nt/2\pi \approx 30$ (see corresponding contour plot). Afterwards, with increasing time, the region grows until saturation sets in again after

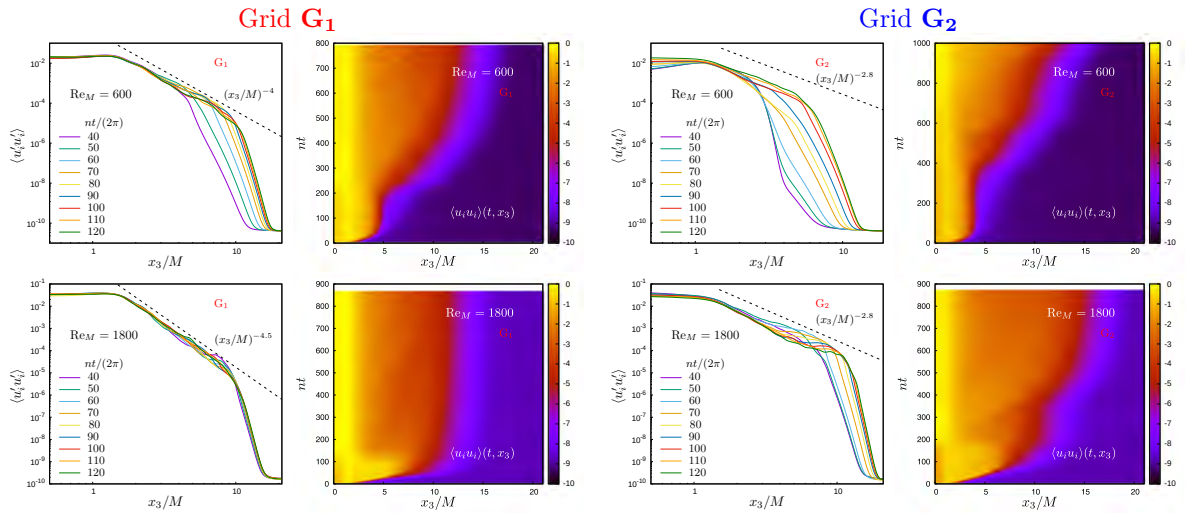

Figure 3: Profiles of second-order velocity moments as a function of distance from the grid. Three regions are visible: a homogeneous core close to the grid, a convective transport region with algebraic decay, and an interfacial zone where energy decreases exponentially. Grid type and Reynolds number control both the extent of the core and the onset of the exponential regime. The decay law with normalized distance x_3/M for the second-order moments are depicted using dashed lines.

$nt/2\pi > 90$. There, its extent is similar to that observed at a much higher Reynolds number of Re_M=1800. Contrary to the lower Reynolds number case, for Re_M=1800 the growth of the convective transport region occurs quickly and is finished already for $nt/2\pi < 40$. Afterwards, hardly any further development of the convective region is observed. The behavior is different for grid G_2. After the initial growth of the convective zone a first saturation of the extent of the convective transport region is still observed and lasts approximately twice as long compared to grid G_1, before the region starts to grow again and saturates after $nt/2\pi \approx 100$. At higher Reynolds number, the initial growth is slower and the intermediate saturation lasts much shorter in time. The final growth of the convective transport region finally leads to a larger extension away from the grid than for grid G_1 and the onset of exponential decay shifts outward. Grid geometry therefore plays a role: G_1 produces a stronger core and a delayed transition to exponential decay, whereas G_2 promotes a faster approach to the far-field regime. These results highlight the sensitivity of oscillating-grid turbulence to the details of the forcing.

The decay of second-order moments with distance from the grid has been the subject of several experimental investigations. McCorquodale & Munro [9] reported $u_{rms} \sim x_3^{-\gamma}$ with $\gamma \simeq 1$, though with considerable scatter across Reynolds numbers (10^3–7×10^3). Zarcos et al. [10] obtained similar results but also proposed a more complex algebraic form to describe the moments in the full water column. Li et al. [11] emphasised the variability of the decay exponent, while Wan [12] documented values between 0.93 and 1.43 depending on the stroke ratio.

Our results are consistent with these observations, reproducing an approximate power-law decay of the root mean square u_{rms} in the convective region, followed by a more rapid exponential regime in the far field, even if the exponent does not match, as in the convective region the energy decays with an exponent between 4 and 4.5 for grid G_1 and around 2.8 for grid G_2, so that the exponent γ of the root mean square ranges between 2 and 2.25 for grid G_1 and around 1.4 for grid G_2 (see Figure 3). Reducing the blocking ratio of the grid, i.e. moving from grid G_1 to grid G_2, produces a clear reduction of the power-law decay, leading to values falling in the range observed by Wan *et al.* [12]. The existence of the three-zone structure helps reconcile the scatter reported in the literature: different studies may probe different zones of the flow or may be affected by forcing-dependent transitions that obscure a universal scaling. Furthermore, a weak dependence on the Reynolds number Re_M can be observed, suggesting that further investigations are needed to determine the amount of variation with Re_M in more detail.

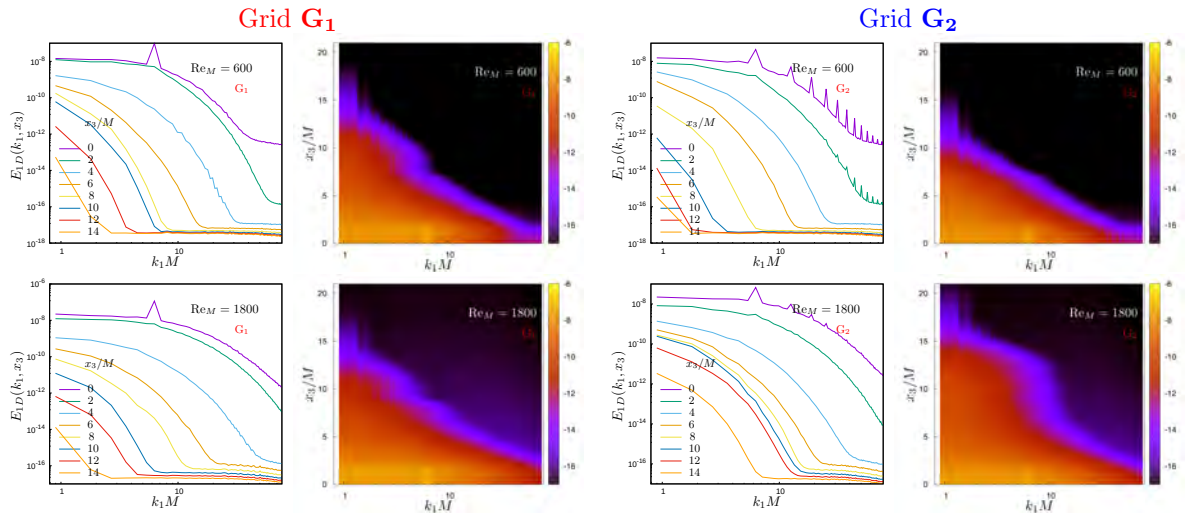

Figure 4: One-dimensional energy spectra at increasing distances from the grid. Close to the grid, spectra exhibit an inertial subrange compatible with Kolmogorov scaling. Further away, universal features progressively deteriorate and the spectra reflect the direct imprint of the forcing.

3.3 Spectral characteristics

One-dimensional velocity spectra at different downstream distances are presented in Figure 4. Within the homogeneous core, approximately up to $x_3/M \lesssim 3$, the spectra develop an inertial subrange compatible with Kolmogorov scaling. This confirms that the turbulence here is well-developed, with energy cascading efficiently from large to small scales. The persistence of this scaling range across Reynolds numbers supports the interpretation of a quasi-stationary turbulent state in the central region.

Further away from the grid, the spectral slopes become strongly dependent on the forcing details. The collapse onto a Kolmogorov-type inertial range progressively deteriorates, and the spectral content reflects the direct imprint of the grid motion. This transition from universal to forcing-dependent behavior marks a second manifestation of the three-zone structure already discussed for the energy profiles.

3.4 Coherent vorticity extraction using orthogonal wavelets

The core idea of coherent vorticity extraction (CVE) is to denoise the vorticity field, $\boldsymbol{\omega}(\boldsymbol{x}) = \nabla \times \boldsymbol{V}$, in wavelet space. The vorticity field is given on a grid (x_i, y_i, z_i) for $i, j, k = 0, N-1$ with $N = 2^{3J}$, where J is the corresponding number of octaves, defining the scales from the largest, $l_{\max} = 2^0$, to the smallest one, $l_{\min} = 2^{1-J}$. The wavelet coefficients threshold is calculated using the parameter ε determining which coefficients correspond to coherent and the incoherent parts. The value of ϵ depends solely on the total enstrophy $Z = \langle \boldsymbol{\omega} \cdot \boldsymbol{\omega} \rangle / 2$ and the total number of points on the grid N and is defined as $\epsilon = \sqrt{4 \cdot Z \cdot \ln(N)}$. The choice of ϵ is based on Donoho's theorem [13]. The implementation of the wavelet

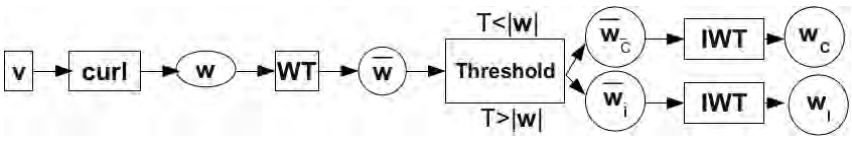

Figure 5: Schematic presentation of the principles of coherent vorticity extraction.

analysis follows several steps (see the sketch in Figure 5): First, after using the fast wavelet transform (FWT), the vorticity wavelet coefficients Ω are calculated ($\Omega = \sqrt{\sum_{\ell=1}^{3} (\tilde{\omega}^{\mu}_{j,i_x,i_y,i_z})^2}$ and $\tilde{\omega}^{\mu}_{j,i_x,i_y,i_z}$). We reconstruct the coherent vorticity $\boldsymbol{\omega}_c$ from those wavelet coefficients for which $\Omega > \epsilon$. The remaining weak wavelet coefficients comprise the incoherent vorticity $\boldsymbol{\omega}_i$. The parameter ϵ provides the initial threshold. A new threshold is obtained from the incoherent enstrophy using weak wavelet coefficients instead of the total enstrophy. The threshold is applied again, and improved coherent and incoherent vorticity

estimators are obtained. The inverse wavelet transform (IWT) reconstructs coherent and incoherent vorticities in physical space. The result of the above operation is the decomposition of $\boldsymbol{\omega}$ into coherent parts $\boldsymbol{\omega}_c$ and incoherent parts $\boldsymbol{\omega}_i$. Further details about the wavelets method can be found in the papers [14, 15, 16, 17, 18] and in the references therein.

The coherent part of vorticity retains almost all of the total energy and enstrophy. In contrast, the incoherent part of vorticity is less organized without exhibiting coherent structures. Although the incoherent part of the vorticity is represented by the majority of wavelet coefficients (more than 97%), it retains a negligible amount of energy (see Table 3.4 for statistics). Here we provide only the statistics for Grid G_1, because the statistics for G_2 are very similar to the presented values. The results are presented in Figure 6 for Reynolds number, $Re = 1800$ and both types of grids G_1 and G_2. The wavelet

Re_M	Grid	Coeff_{coh}	Coeff_{inc}	Energy_{coh}	Energy_{inc}
1800	G_1	2.4%	97.6%	0.98	0.022

Table 1: Statistics of CVE. To note, the values for Grid G_2 are very close the values presented.

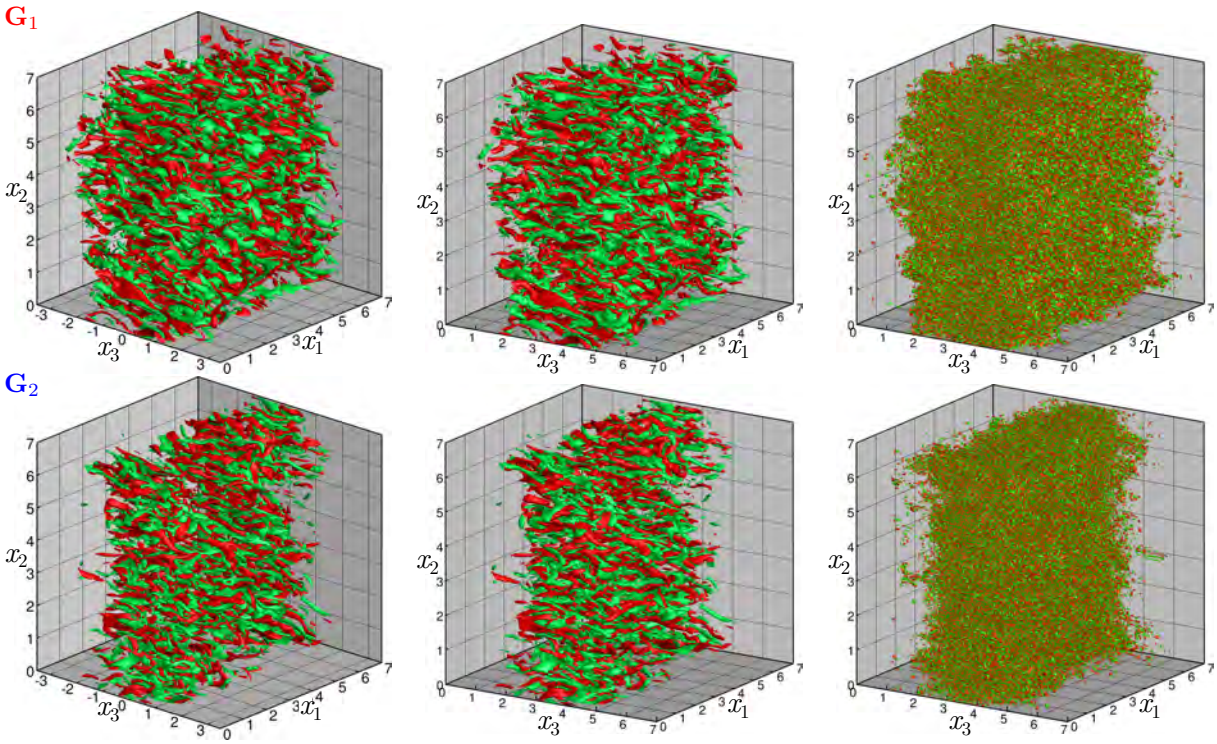

Figure 6: Total (left), coherent (centre), and incoherent (right) fields of ω_z for $Re = 1800$ and Grids G_1 and G_2, upper and lower rows, respectively. Iso-values for total and coherent parts are: $\omega_z = 2.0$, for incoherent part $\omega_{z,\mathrm{inc}} = 0.3$.

decomposition of the vertical vorticity component, shown in Figure 6, separates the flow into coherent and incoherent contributions.

The incoherent part is found to decay rapidly outside the central region, leaving only the coherent structures associated with the grid forcing. This behavior confirms that, away from the homogeneous core, turbulence does not follow a universal cascade but is dominated by persistent coherent motions linked to the geometry and oscillation of the grid. This observation provides a structural interpretation of the energy decay laws: the far-field flow is not simply a self-similar turbulent decay but a superposition of coherent structures of grid origin and a rapidly vanishing background of small-scale turbulence.

The probability density functions (PDF) of the coherent and incoherent parts of the vorticity are presented in Figure 7, for Re_M=1800, exemplarily. PDFs' total vorticity fields are not shown because they fully superimpose on PDFs' total component. For both coherent and incoherent parts, G_1 has

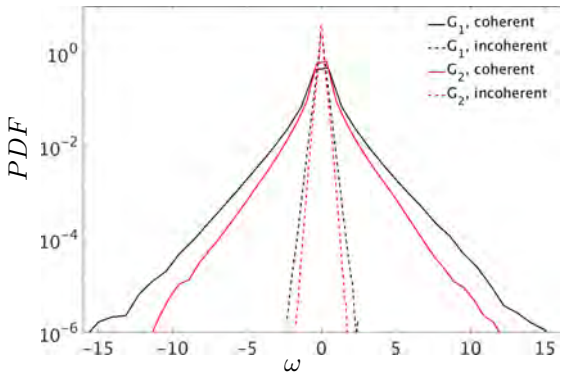

Figure 7: PDFs of coherent and incoherent vorticity fields for $Re_M = 1800$. Black and red lines correspond to Grids G_1 and G_2. Solid and dashed lines to coherent and incoherent parts, respectively.

broader tails than G_2, which means that Grid G_1 produces a turbulent flow with stronger intermittency and more intense coherent vortices compared to Grid G_2.

4 Discussion and Conclusions

The numerical experiments presented here provide new insight into the long-standing problem of turbulence generated by oscillating grids. While the flow exhibits several features that resemble canonical turbulence — such as a homogeneous central core and spectra compatible with Kolmogorov scaling — our results highlight the crucial role of the forcing details in shaping the asymptotic state.

A central outcome is that the turbulence generated in this way is not universal: even at high Reynolds numbers, the flow retains a persistent anisotropy and a measurable imprint of the grid geometry. This implies that oscillating-grid turbulence cannot be regarded as a substitute for freely decaying homogeneous isotropic turbulence, but rather as a distinct flow whose properties must be characterised on their own.

These findings provide a useful perspective on the diversity of experimental scaling laws. For example, the power-law decay $u_{rms} \sim x_3^{-\gamma}$ with $\gamma \simeq 1$ reported by McCorquodale & Munro [9] and the alternative rational law of Zarcos *et al.* [10] can be reconciled if one accepts that the exponent (or the functional form) is not universal but depends on the grid parameters and the forcing strategy. The variability in exponents reported by Li *et al.* [11] and Wan *et al.* [12] is consistent with our observation that changes in the blocking ratio and stroke length modify the balance between transport and dissipation in the intermediate region.

From a methodological point of view, the simulations confirm the practicality of using localized body forces to represent oscillating grids. The approach is flexible enough to encode different grid geometries and oscillation parameters while avoiding the prohibitive cost of resolving the moving structure. At the same time, the persistence of coherent structures in the far-field demonstrates that the details of the forcing cannot be ignored: grid-forced turbulence is shaped as much by how energy is injected as by how it is dissipated.

In conclusion, oscillating-grid turbulence should be viewed not as a universal model for isotropic turbulence, but as a reproducible laboratory and numerical configuration that combines approximate homogeneity with a tunable imprint of its forcing mechanism. Its value lies precisely in this balance: It provides a controllable test bed to investigate diffusion, entrainment, and mixing in inhomogeneous turbulent flows. Future work should extend the parameter space, in particular, varying the Reynolds number and the stroke-to-mesh ratio independently, to clarify the transition between forcing-dominated and transport-dominated regimes, and to provide a unified framework for interpreting the different empirical scaling laws reported in the literature.

5 ACKNOWLEDGMENTS

The authors thank the Deutsche Forschungsgemeinschaft (DFG) for support for a research visit of Michele Iovieno at Siegen (FO 67420-1). Furthermore we thank the computer center of the University of Siegen (ZESS) for calculation time on OMNI cluster. George Khujadze acknowledges M. Farge and K. Schneider for their insightful discussions regarding the wavelet theory over the years.

References

[1] H.J.S. Fernando. Turbulent mixing in stratified fluids. *Annu. Rev. Fluid Mech.*, 23:455–493, 1991.

[2] S.J. Bennett and J.L. Best. Particle size and velocity discrimination in a sediment-laden turbulent flow using phase doppler anemometry. *J. Fluids Eng.*, 117:505–511, 1995.

[3] E. Hopfinger and J. Toly. Spatially decaying turbulence and its relation to mixing across density surfaces. *J. Fluid Mech.*, 78:155–177, 1976.

[4] E. Hopfinger, F. Browand, and Y. Gagne. Turbulence and waves in a rotating tank. *J. Fluid Mech.*, 125:505–534, 1982.

[5] I. De Silva and H. Fernando. Oscillating grids as a source of nearly isotrpoic turbulence. *Phys. Fluids*, 6(7):2455–2464, 1994.

[6] G. Yang. DNS of boundary forced turbulent flow in a non-rotating and rotating system. *Ph.D. thesis, Cornell University*, 1992.

[7] F. S. Godeferd and L. Lollini. Direct numerical simulations of turbulence with confinement and rotation. *J. Fluid Mech.*, 393:257–308, 1999.

[8] M. Iovieno, C. Cavazzoni, and D. Tordella. A new technique for a parallel dealiased pseudespectral navier-stokes code. 141:365–374, 2001.

[9] M. W. McCorquodale and R. J. Munro. Experimental study of oscillating-grid turbulence interacting with a solid boundary. *J. Fluid Mech.*, 813:768–798, 2017.

[10] M. Poulain-Zarcos, M. J. Mercier, and A Halle. Global characterization of oscillating grid turbulence in homogeneous and two-layer fluids, and its implication for mixing at high Peclet number. *Phys. Rev. Fluids*, 7:054606, 2022.

[11] W. Li, P. Zhang, S. Yang, X. Fu, and Xiao Y. An experimental method for generating shear-free turbulence using horizontal oscillating grids. *Water*, 12:591, 2020.

[12] W.H.M. Wan Mohtar. Oscillating-grid turbulence at large strokes: Revisiting the equation of Hopfinger and Toly. *J. Hydrodynamics*, 48:473–481, 2016.

[13] D. Donoho. Unconditional bases are optimal bases for data compression and statistical estimation. *Appl. Comput. Harmon. Anal.*, 1:100–115, 1993.

[14] M. Farge. Wavelet transforms and their applications to turbulence. *Annu. Rev. Fluid Mech.*, 24:395, 1992.

[15] K. Schneider and O. Vasilyev. Wavelet methods in computational fluid dynamics. *Annu. Rev. Fluid Mech.*, 42:473, 2010.

[16] T. Sakurai, K. Yoshimatsu, K. Schneider, M. Farge, K. Morishita, and T. Ishihara. Coherent structure extraction in turbulent channel flow using boundary adapted wavelets. *Journal of Turbulence*, 18(4):352–372, 2017.

[17] G. Khujadze, K. Ritos, I.W. Kokkinakis, D. Drikakis, and S.M. Spottswood. Wavelet analysis of high-speed transition and turbulence over a flat surface. *Physics of Fluids*, (34):046107, 2022.

[18] I.W. Kokkinakis, G. Khujadze, D. Drikakis, and S.M. Spottswood. Wavelet analysis of supersonic shock-boundary-layer interaction. *Physics of Fluids*, (34):066106, 2023.